Available online at www.sciencedirect.com
ScienceDirect
Journal of Power Sources 171 (2007) 652–662
JOURNAL OF POWER SOURCES
www.elsevier.com/locate/jpowsour

Metallic interconnects for SOFC: Characterisation of corrosion resistance and conductivity evaluation at operating temperature of differently coated alloys

S. Fontana [a,*], R. Amendola [b], S. Chevalier [a], P. Piccardo [b], G. Caboche [a], M. Viviani [c], R. Molins [d], M. Sennour [d]

[a] *Institut Carnot de Bourgogne, UMR 5209 CNRS, Université de Bourgogne, 9 Avenue Alain Savary, BP 47870, F-21078 Dijon Cedex, France*
[b] *DCCI, Universita di Genova, via Dodecaneso 31, I 16146 Genova, Italy*
[c] *IENI, CNR Genova Area, Via de Marini, I 16149 Genova, Italy*
[d] *ENSMP, Centre des Matériaux, UMR-CNRS 7633, F 91003 Evry, France*

Received 20 February 2007; received in revised form 31 May 2007; accepted 24 June 2007
Available online 5 July 2007

Abstract

One of challenges in improving the performance and cost-effectiveness of solid oxide fuel cells (SOFCs) is the development of suitable interconnect materials. Recent researches have enabled to decrease the operating temperature of the SOFC from 1000 to 800 °C. Chromia forming alloys are then among the best candidates for interconnects. However, low electronic conductivity and volatility of chromium oxide scale need to be solved to improve interconnect performances. In the field of high temperature oxidation of metals, it is well known that the addition of reactive element into alloys or as thin film coatings, improves their oxidation resistance at high temperature. The elements of beginning of the lanthanide group and yttrium are the most efficient. The goal of this study is to make reactive element oxides (La_2O_3, Nd_2O_3 and Y_2O_3) coatings by metal organic chemical vapour deposition (MOCVD) on Crofer 22 APU, AL 453 and Haynes 230 in order to form perovskite oxides which present a good conductivity at high temperature. The coatings were analysed after 100 h ageing at 800 °C in air under atmospheric pressure by scanning electron microscopy (SEM), energy dispersive X-ray (EDX) analyses, X-ray diffraction (XRD) and transmission electron microscopy (TEM) analyses. Area-specific resistance (ASR) was measured in air for the same times and temperature, using a sandwich technique with Pt paste for electrical contacts between surfaces. The ASR values for the best coating were estimated to be limited to 0.035 Ω cm^2, even after 40,000 h use.
© 2007 Elsevier B.V. All rights reserved.

Keywords: SOFC; Reactive element; Interconnect; MOCVD; ASR

1. Introduction

Significant progress in the research and development of solid oxide electrochemical devices to convert chemical reaction energy directly into electrical energy without combustion process have been made for several years. The solid oxide fuel cells (SOFCs) seem the most efficient way to generate electricity from a variety of fuel such as hydrogen, methane or even natural gases owing to their high operating temperatures typically in the range 800–1000 °C. Moreover, high operating temperature favors rapid reaction kinetics and allows reforming of hydrocarbon fuels within the fuel cell (internal reforming). In addition, SOFCs generate very low levels of pollutants with a high power density. A SOFC is composed of two porous electrodes, an anode and a cathode, separated by a gas imperviousness ion-conducting electrolyte. The interconnect provides electrical connection between anode of one individual cell to the cathode of the neighbouring one. It also acts as physical barrier to avoid any contact between the reducing and the oxidising atmospheres. In order to perform their intended functions, interconnects should have the following characteristics [1–3]:

- Excellent electrical conductivity. The acceptable area-specific resistance (ASR) level is considered to be below 0.1 Ω cm^2;

* Corresponding author. Tel.: +33 3803 96158; fax: +33 3803 96132.
E-mail address: sebastien.fontana@u-bourgogne.fr (S. Fontana).

0378-7753/$ – see front matter © 2007 Elsevier B.V. All rights reserved.
doi:10.1016/j.jpowsour.2007.06.255

- Adequate stability in terms of dimensions, microstructure, chemistry and phases at operating temperature around 800 °C in both oxidising and reducing atmospheres during 40,000 h (service lifetime);
- Excellent imperviousness for oxygen and hydrogen to prevent direct combination of oxidant and fuel during operating;
- Thermal expansion coefficient (TEC) matching those of electrodes and electrolyte, around $10.5 \times 10^{-6}\,K^{-1}$, so that the thermal stresses developed during start-up and shut down could be minimized;
- No reaction or interdiffusion between interconnect and its adjoining components;
- Fairly good thermal conductivity; $5\,W\,m^{-1}\,K^{-1}$ is considered to be the lowest limit;
- Excellent oxidation, sulfidation and carbon cementation resistance;
- Adequate strength and creep resistance at elevated temperatures;
- Ease to fabrication and shaping, as well as a low cost.

Traditional SOFCs work at high temperature, around 1000 °C. At this temperature, the interconnect material is conventionally made of a ceramic material, such as $La_{1-x}Ca_xCrO_3$ [4]. However, these ceramic interconnects are difficult to manufacture, which limits the application in SOFCs. Ceramic interconnects also have low electrical conductivity and are expensive.

Recent research has enabled to decrease the operating temperature of the SOFC from 1000 to 800 °C. This progress has been made by reducing the thickness of the electrolyte [5] and improving the cathode electrolyte interface reaction (i.e. triple phases boundaries (TPB) to internal diffusion (ID) mechanism) [6]. The lower operating temperature authorises metallic alloys as possible candidates for interconnects [4]. Metallic materials have higher electrical and thermal conductivities, are easier to fabricate, and, in general, have lower cost compared to the ceramic interconnects [4,7].

Cr is the most important element because of the formation of chromia as protective and semiconducting layer. The presence of other elements could improve the characteristics of this layer, limiting the growth rate and the ASR, reducing the poisoning of the electrodes due to the oxidation gaseous species (CrO_3 or $CrO_2(OH)_2$) at temperatures close to 1000 °C and higher [8–10], but also observed at lower temperatures due to the severe operation conditions, such as the presence of water vapour [8,9,11,12]. The formation of a protective, single-phase chromia layer requires chromium content of approximately 17–20% [7,13–15], depending on temperature, on surface treatment and on minor alloying additions. Mn and Ti are used in a few tenths of the percent to improve the oxidation resistance. Mn tends to form a Cr–Mn spinel on the external surface layer to decrease the formation of volatile Cr species [7,8,14,16–18]. Elements such as molybdenum and tungsten can also be added to match better thermal expansion coefficient of the alloys to those of other fuel cell components. The amount of aluminum and silicon must be kept low to prevent the formation of their insulating oxides, alumina and silica.

The use of reactive element is known to improve both the electrical conductivity and the oxidation resistance of all chromia-forming alloys [14,19,20]. Their main role consists in changing the diffusion mechanism during the chromia scale formation from outward diffusion of the chromium ions to inward diffusion of the oxygen ions. Without reactive elements, vacancies are formed at the metal/oxide interface leading to scale cracking and spalling [14,19,21,22]. In presence of reactive elements, the adhesion of the chromia scale is improved, the oxidation rate is decreased, the Cr vaporisation is limited and the electric conductivity is increased [14,22,23,24].

As an alternative approach to the bulk modification of alloys, a metallic interconnect can be surface-modified via a protective oxide layer. Coating systems were developed in order to reduce Cr vaporisation, to reduce electric resistance and to improve corrosion resistance [25,26]. They mostly consisted of perovskite layers on the bases of $(La,Sr)MnO_3$ or $(La,Sr)CrO_3$ [13,20,26,27,28]. More recently tests were performed with spinel coatings especially $(Co,Mn)_3O_4$ [26,29–31]. Qu et al. [32] deposited sol–gel coating of 200 nm thick, containing Y/Co or Ce/Co, on AISI430. These coatings exhibit lower oxidation rate relative to the uncoated steel; Y/Co coating gives the best results. Alman and Jablonski [33] deposited Ce on Crofer 22 APU by pack cementation. The treatment appeared to decrease the electrical resistance of the oxide scale.

At high temperature, the reactive elements which present the best efficiency on the alloys are the elements of the beginning of the lanthanide group and the yttrium [14,34]. That is the reason why, in this study, La_2O_3, Nd_2O_3 and Y_2O_3 coatings were deposited on different metallic alloys (Crofer 22 APU, AL 453 and Haynes 230) by metal organic chemical vapour deposition (MOCVD) technique in order to form perovskite oxides at high temperature. Isothermal oxidation experiments were performed at 800 °C for 100 h in air under atmospheric pressure. The coatings and the corrosion products were carefully analyzed by scanning electron microscopy (SEM), energy dispersive X-ray (EDX) analyses, X-ray diffraction (XRD) and transmission electron microscopy (TEM).

2. Experimental

2.1. Sample preparation

Two ferritic stainless steels, Crofer 22 APU and AL 453, were investigated. A Ni-based alloy, Haynes 230, was also tested for comparison. The nominal compositions of the three alloys are given in Table 1. Crofer 22 APU was provided by ThyssenKrupp VDM, AL 453 by Alleghany Ludlum and Haynes 230 by Haynes International. Despite its CTE which is higher than that of other components of the cell, Haynes 230 was chosen in order to anticipate eventual change of the electrodes/electrolyte materials. Also, as it was largely studied in the past [35–37], one can consider the influence of the coatings on the oxidation as well as on the electrical behaviour. It seams then interesting to compare the oxidation and the resistivity of this Ni-base materials with ferritics materials.

Table 1
Alloy composition in weight (%)

Wt.%	Al	C	Cr	Co	Fe	Mn	Mo	Ni	P	S	Si	Ti	W	RE
Crofer 22 APU	–	0.005	22	–	Bal	0.5	–	–	0.016	0.002	–	0.08	–	0.06 (La)
AL 453	0.6	0.03	22	–	Bal	0.3	–	0.3	0.02	0.03	0.3	0.02	–	0.10 (La,Ce)
Haynes 230	0.4	0.1	22	5	3	0.5	1.26	Bal	0.005	0.002	0.4	–	14	0.02 (La)

The samples were cut in squares of 1 cm of side and about 2 mm of thickness; prior to deposition, the samples were polished from 240-grit silicon carbide up to 1 μm with diamond paste. They were finally cleaned in ethanol in an ultrasonic bath and dried.

Three reactive element coatings were chosen: La_2O_3, Y_2O_3 and Nd_2O_3. The coatings of reactive element oxides were applied on the alloys by the metal organic chemical vapour deposition (MOCVD) technique [34,38,39]. β-Diketonate powders (tris-2,2,6,6-tetramethyl-3,5-heptanedionato (tmhd) La, Y or Nd) were used as metal–organic precursors; their syntheses were performed in the laboratory and described in ref. [40].

The multi-sources MOCVD apparatus is schematized in Fig. 1 It is composed of:

- Three metal organic sources (A, B, C);
- A quartz reactor heated by infrared (IR) furnace;
- A vacuum system allowing the MOCVD process at low pressure;
- Mass flow meters to control N_2 (carrier gas for precursors) and O_2 flow rates.

The samples were placed horizontally on a metallic sample holder inside the cold-wall reactor. In the IR-heated reactor, precursors were pyrolyzed inside a small volume, just above the heated substrate. Nitrogen gas was used as carrier gas for metal organic precursors. Oxygen was used as oxidant and was incorporated to the main flow via an intermediate mixing chamber. The gaseous mixture was then directed to the reaction chamber through a nozzle. The precursor delivery lines were heated and maintained at a temperature higher than the source evaporation line, to prevent condensation of the metal–organic vapour phase.

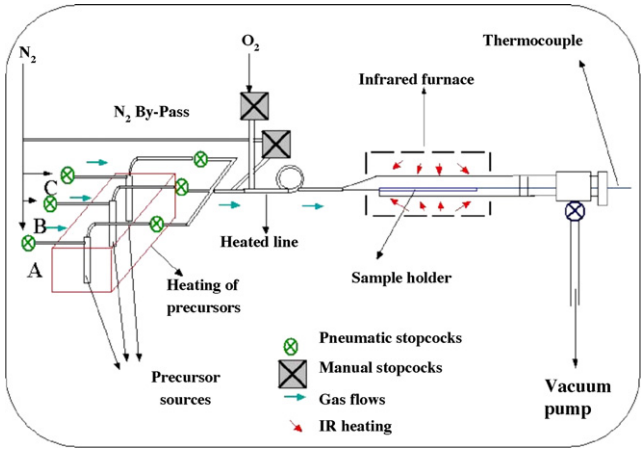

Fig. 1. Diagram of the MOCVD apparatus.

The conditions of deposition are described in Table 2. This technique enables to form thin nanostructured oxide films of about 100–200 nm thick [38].

The surface of the alloys after deposition of La_2O_3, Nd_2O_3 and Y_2O_3 were observed by scanning electron microscopy (SEM)/energy dispersive X-ray (EDX) analyses on both faces prior to the oxidation tests. The coating surface did not exhibit crystallites, it showed a very smooth appearance and the reactive element (La, Nd or Y) associated with O were detected by EDX. In addition the elements of the alloy (Cr, Fe or Ni) are detected, that means that the coating has a small thickness. X-ray diffraction (XRD) analyses, using Kα (λ = 0.154 nm) copper radiation, were performed at 1° glancing angle in order to get information from the deposited thin films. These experiments reveal the presence of La_2O_3 (ICDD card no. 05-0602) for the La_2O_3 coating, Nd_2O_3 (ICDD card no. 04-1280) for the Nd_2O_3 coating and Y_2O_3 coating (ICDD card no. 41-1105). The diffraction peaks appear very large, probably because the grains of the coatings have a nanometric size and/or because the coatings are not fully crystallised.

2.2. Oxidation tests and oxide scale analyses

Uncoated and coated sample behaviour were studied at 800 °C in air (laboratory air) under atmospheric pressure for 100 h. The growth of the chromia scale generally obeys the parabolic rate law, according to the following equation [14,41].

$$\left(\frac{\Delta m}{A}\right)^2 = k_p t$$

where Δm is the mass gain of the sample (g), A the total oxidized area of the sample (cm^2), k_p the parabolic rate law constant ($g^2\ cm^{-4}\ s^{-1}$) and t is the oxidation time (s).

During these experiments, the samples were submitted to thermogravimetric analyses (using a Setaram TGA 92) in order to get the oxidation kinetics. The parabolic rate law was verified by plotting $\Delta m/A$ versus $t^{1/2}$ [41], whose slopes enabled to evaluate the parabolic rate law constants, k_p. Deviation from

Table 2
Coating conditions during the MOCVD process

	La_2O_3	Y_2O_3	Nd_2O_3
Precursor sources	A	B	C
Precursor temperature	200	215	230
Substrate temperature	600	600	600
N_2 flow rate ($1\ h^{-1}$)	7.5	7.5	7.5
O_2 flow rate ($1\ h^{-1}$)	2.5	2.5	2.5
Total pressure in reactor (mbar)	2	2	2

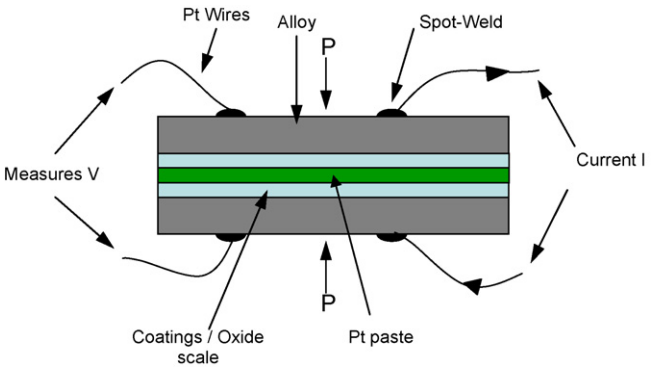

Fig. 2. Diagram representation of the ASR measurement method.

parabolic law was sometimes observed. The thickness of the oxide scale was estimated, assuming that the scale is mainly composed of pure dense chromia (density 5.2 g cm^{-3}).

The surface oxide morphologies were observed using a "JEOL JSM-6400F" scanning electron microscope (SEM) equipped with a field emission gun (FEG). This device coupled with an energy dispersive X-ray spectrometer was used to determine the morphology and the analysis of the corrosion products. Since, the oxide scales were very thin after 100 h at 800 °C, SEM cross-sections were realised only on the uncoated AL 453.

The oxides formed after ageing were also characterized by X-ray diffraction (XRD) using Cu Kα (λ = 0.154 nm) radiation with an incident angle of 1°.

Cross-sectioned samples were investigated using analytical transmission electron microscopy (TEM) with a nanometric analytical resolution (Tecnai F20 ST) in order to characterize the morphology and the chemistry of the oxide scales developed on uncoated and coated samples after 100 h at 800 °C in air.

2.3. Electrical conductivity measurement

The electrical resistivity measurements of the oxidized alloy were performed on uncoated and coated samples. Two identical samples were bonded together on one face with a mixture of Pt paste and α-terpinol to obtain a sandwich; they were connected to the measurement instrumentation by two Pt wires per each sample spot-welded on the opposite side (Fig. 2). The surface of these sides was polished in order to remove the oxide scale. Electrical resistance was then estimated by the voltage value measured applying three different intensities of current (i.e. 100, 150, 200 mA) at 800 °C during 100 h; the average resistance R is then considered as the double of the corresponding resistance of the scale formed on the surface of the two sandwiched samples.

The area-specific resistance (ASR) parameter reflects the resistance, the thickness, as well as the electrical properties of the oxide layers. The calculation of the oxide-layer resistivity requires correct measurement of the thickness. It is generally accepted that the resistivity of the alloy substrate is negligible compared to that of the thermally grown oxide layer [8]. From the definition of the ASR parameters, Huang et al. [8] established a relation between the ASR and the time t:

$$\mathrm{ASR} = 2\frac{M_{Cr_2O_3} \times \sqrt{k_p \times t}}{(3 \times M_O \times \rho_{Cr_2O_3}) \times \sigma}$$

where σ is the total conductivity of the oxide layer in S cm^{-1}, k_p the parabolic rate law constant, $M_{Cr_2O_3}$ and M_O the molar mass of chromia and of the oxygen, respectively, $\rho_{Cr_2O_3}$ the density of chromia and t is the exposure time. The factor 2 is due to the fact that in our case, two samples were measured face to face together.

3. Results

3.1. Oxidation behaviour of uncoated and coated Crofer 22 APU

Kinetics of scale formation on Crofer 22 APU, with different coatings and after ageing at 800 °C for 100 h in air at atmospheric pressure are presented in Fig. 3. All specimens obey a parabolic rate law, even if the shape of the mass gain curves looks wavy. The parabolic rate constants deduced from these curves are reported in Table 3. The k_p of the uncoated Crofer 22 APU in our case is closed to the k_p found by Huczkowski et al. [42]. Whatever the coatings, the oxidation resistance is equally improved. If compared with the uncoated sample, the mass gain is reduced of approximately 35% for coated specimens. The calculated chromia scale thickness is then decreased by a factor 1.5 when a coating is applied. In this case, the coating effect does not depend on the nature of the reactive element. In addition, the presence of reactive element on the surface seems to decrease the amplitude of waves on the kinetic curves.

Fig. 4 shows the surface morphologies of uncoated and La_2O_3, Y_2O_3, Nd_2O_3-coated samples aged for 100 h in air under atmospheric pressure at 800 °C. The surface of the uncoated sample is rather homogeneous. The microstructure of the outer grains looked like typical spinel phases, covering an underscale composed of smaller grains, probably chromia according

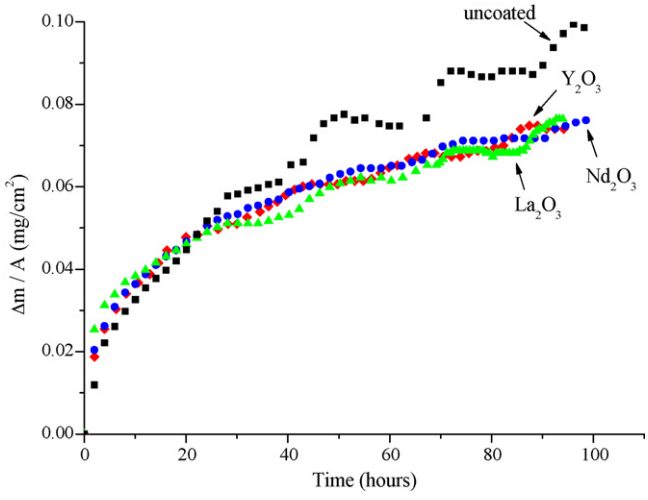

Fig. 3. Kinetics (for 100 h) of coated and uncoated Crofer 22 APU at 800 °C in air under atmospheric pressure.

Table 3
Values of the parabolic rate constants k_p and thicknesses of the oxide scales for coated and uncoated samples of Crofer 22 APU, AL 453 and Haynes 230 after 100 h at 800 °C in air under atmospheric pressure

Alloy	Coating	k_p ($g^2\,cm^{-4}\,s^{-1}$)	Oxide thickness (nm)
Crofer 22 APU	Without coatings	4.8×10^{-14}	730
	La_2O_3 coating	0.9×10^{-14}	451
	Nd_2O_3 coating	1.0×10^{-14}	463
	Y_2O_3 coating	1.1×10^{-14}	469
AL 453	Without coatings	3.9×10^{-13}	2370
	La_2O_3 coating	1.6×10^{-14}	490
	Nd_2O_3 coating	6.9×10^{-14}	1020
	Y_2O_3 coating	1.1×10^{-13}	1040
Haynes 230	Without coatings	2.8×10^{-15}	244
	La_2O_3 coating	1.7×10^{-15}	195
	Nd_2O_3 coating	2.7×10^{-15}	225
	Y_2O_3 coating	5.9×10^{-15}	274

Table 4
Phases identified by XRD analyses on the surface of uncoated and coated samples of Crofer 22 APU, AL 453 and Haynes 230 after 100 h at 800 °C in air under atmospheric pressure

Alloy	Coating	XRD phases
Crofer 22 APU	Without coatings	Cr_2O_3, $(CrMn)_3O_4$
	La_2O_3 coating	Cr_2O_3, $LaCrO_3$, $(CrMn)_3O_4$
	Nd_2O_3 coating	Cr_2O_3, $NdCrO_3$, $(CrMn)_3O_4$
	Y_2O_3 coating	Y_2O_3, $(CrMn)_3O_4$
AL 453	Without coatings	Cr_2O_3, $(CrMn)_3O_4$
	La_2O_3 coating	Cr_2O_3, $LaCrO_3$, $(CrMn)_3O_4$
	Nd_2O_3 coating	Cr_2O_3, $NdCrO_3$, $(CrMn)_3O_4$
	Y_2O_3 coating	Y_2O_3, $YCrO_3$, $(CrMn)_3O_4$
Haynes 230	Without coatings	Cr_2O_3, $(NiCr)_3O_4$
	La_2O_3 coating	Cr_2O_3, $LaCrO_3$, $(NiCr)_3O_4$, WO_3
	Nd_2O_3 coating	Cr_2O_3, $NdCrO_3$, $(NiCr)_3O_4$
	Y_2O_3 coating	Y_2O_3, $YCrO_3$, Cr_2O_3

to the EDX analyses. For the La_2O_3-coated sample (Fig. 4b), the oxide layers seemed to be thinner as substrate grain boundaries remained visible on the oxidized surface. Fig. 4b shows a triple layered microstructure with a spinel oxide as large crystals on the top surface, covering a widely developed underscale of smaller grains. The third layer is observable on some areas and seems composed of small equiaxed grains.

Table 4 reports the phases identified by XRD analyses on the surface of uncoated and coated samples of Crofer 22 APU after 100 h at 800 °C under atmospheric pressure. For uncoated and coated samples, chromia (ICDD card no. 38-1479) and a spinel phase $(Cr,Mn)_3O_4$ very closed to $Cr_{1.5}Mn_{1.5}O_4$ (ICDD card no. 33-0892) were detected (due to the similarity of the ionic radii of Cr, Mn and/or Fe, it is difficult to determine the exact chemistry of the spinel). The La_2O_3, coated sample showed a perovskite phase, $LaCrO_3$ (ICDD card no. 33-0701), as indicated in Table 4.

STEM cross-section observations were only performed on uncoated and La_2O_3-coated Crofer 22 APU after 100 h ageing. On the uncoated specimen (Fig. 5), a continuous chromia scale was detected at the substrate surface. Some pores were randomly detected within the scale. The chromia layer was covered with large Cr/Mn spinel crystals identified by EDX analysis as $(Cr,Mn)_3O_4$. It is interesting to note that some cracks were

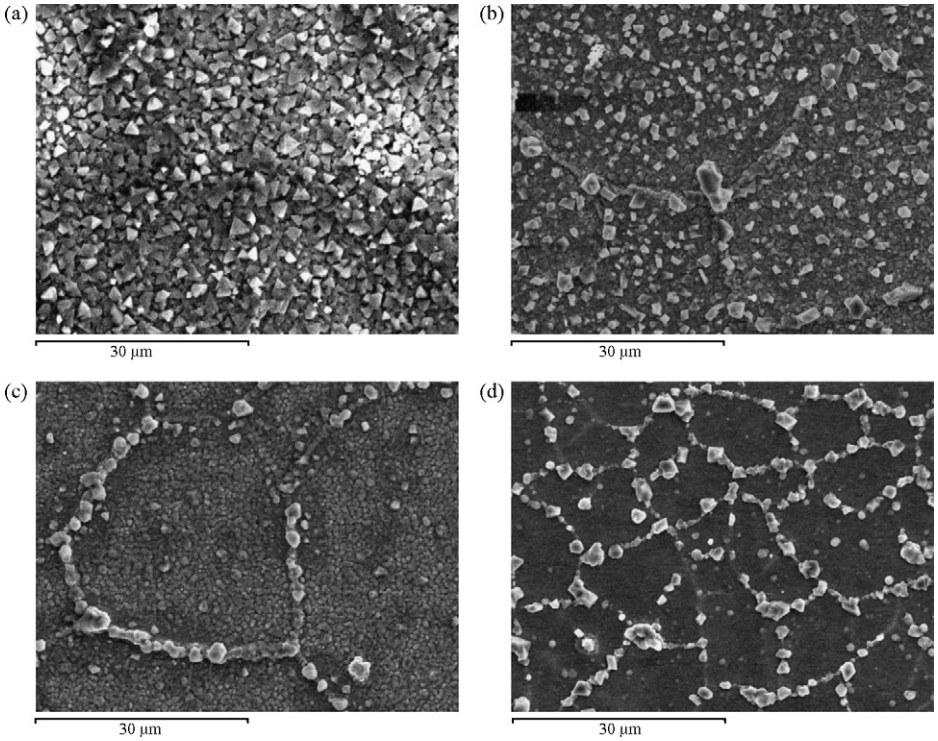

Fig. 4. SEM observations of Crofer 22 APU oxidized in air at 800 °C for 100 h: (a) without coating, (b) with La_2O_3 coating, (c) with Nd_2O_3 coating and (d) with Y_2O_3 coating.

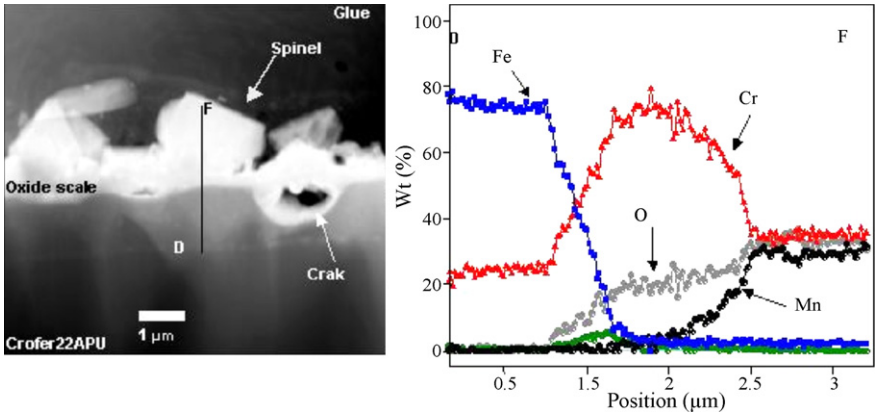

Fig. 5. Uncoated Crofer 22 APU oxidized 100 h at 800 °C: high angle annular dark field (HAADF) image and associated EDX profile from outer oxide to substrate.

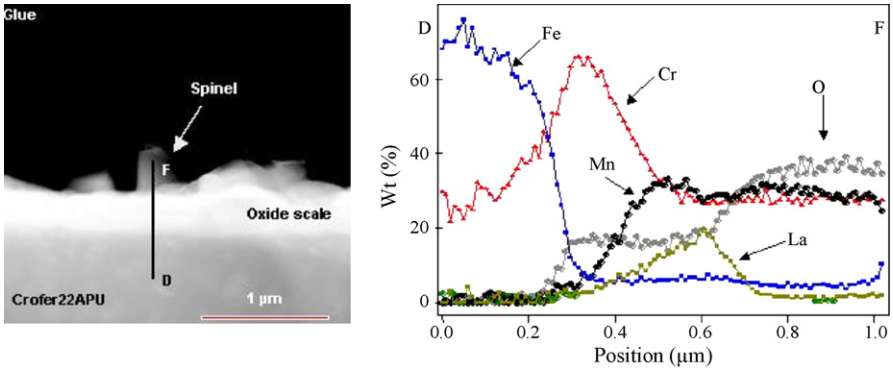

Fig. 6. La_2O_3-coated Crofer 22 APU oxidized 100 h at 800 °C: HAADF image and associated EDX profile from outer oxide to substrate.

detected (see right side of Fig. 5) at the interface between the metallic substrate and the scale. The TEM results are in agreement with XRD identification.

The La_2O_3-coated sample (Fig. 6) displayed a thinner (approximately two times) and more adherent chromia scale. Some spinel grains, of the same composition as for the uncoated sample, were also detected at the outer surface. The element profile acquired on the cross-section of Fig. 6 (all along the black line) showed that the reactive element oxide was concentrated at the interface between the forming chromia layer and the external spinel grains, probably as $LaCrO_3$.

In the case of the Nd_2O_3-coated sample, the morphology (Fig. 4c) and the nature of the crystalline phases (Table 4) are similar to those obtained for the La_2O_3-coated sample. The XRD analyses reveal the presence of a perovskite $NdCrO_3$ (ICDD card no. 39-1429) and a spinel phase.

The morphology of the Y_2O_3-coated sample is very different (Fig. 4d). The surface presents some crystallites of spinel Cr–Mn located at the grain boundaries of the substrate. Between cracks, yttria is mostly present. It seems that perovskite did not form during ageing at 800 °C. In fact, the XRD analyses reveal the presence of yttria (ICDD card no. 41-1105) and spinel phase but no perovskite $YCrO_3$ is detected (Table 4).

The results of thermogravimetry showed that the presence of reactive element oxide on Crofer 22 APU surface decreased the parabolic rate constant. The ASR values were also modified compared to uncoated alloy. But the ASR parameter depends on the selected coating (Fig. 7). In the case of the uncoated alloy, after 100 h at 800 °C, the ASR parameter is equal to 0.086 Ω cm^2. This value is closed to the value found by Quadakkers et al. [43] or found by Yang et al. [17]. It is clear that the La_2O_3 coating improves the electric conductivity of the oxide scale; in fact, after 100 h at 800 °C, the ASR parameter is only 0.004 Ω cm^2. However, the value found for the yttria coating is higher 0.252 Ω cm^2. In the case of Nd_2O_3 coating, there is an improvement of the electric conductivity, but the value of the ASR parameter (0.016 Ω cm^2) is higher than for La_2O_3 coating.

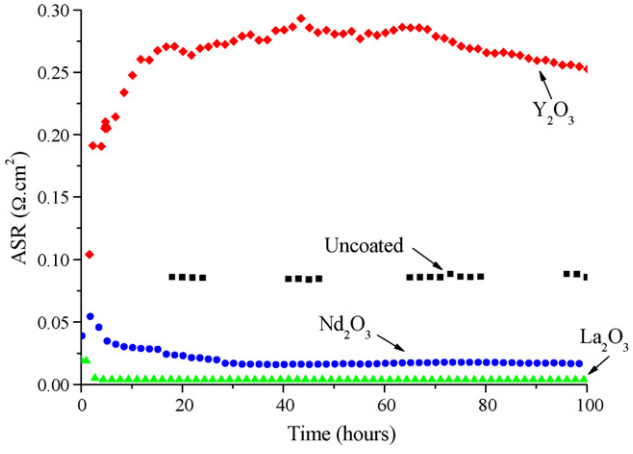

Fig. 7. ASR parameter evolution (for 100 h) of coated and uncoated Crofer 22 APU at 800 °C in air under atmospheric pressure.

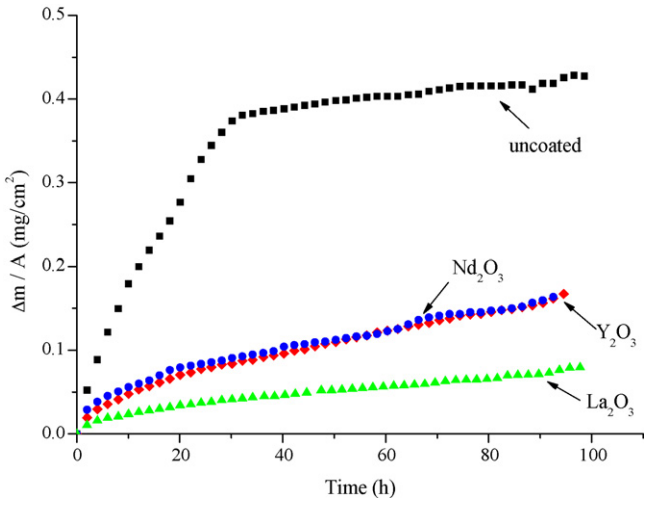

Fig. 8. Kinetics (for 100 h) of coated and uncoated AL 453 at 800 °C in air under atmospheric pressure.

3.2. Oxidation behaviour of uncoated and coated AL 453

As for Crofer 22 APU, the kinetic curves of oxidation of uncoated or coated Al 453 show parabolic kinetics (Fig. 8). In the case of uncoated alloy, the behaviour is not acceptable for its use as interconnector; in fact, the weight gain after 100 h at 800 °C is too high; as a matter of fact, the oxide scale is too thick (Table 3). The k_p value of the uncoated Al 453 in our case is closed to that found by Yang et al. [44]. Contrary to Crofer 22 APU alloy, the effect of the coating depends on the selected reactive element. Indeed, in comparison with uncoated alloys, the La_2O_3 coating acts as beneficial; the mass gain is reduced of approximately 79% as for Nd_2O_3 and Y_2O_3 coatings, the mass gain is only decreased by 56%.

Fig. 9 shows the surface morphologies of uncoated and coated sample aged for 100 h in air under atmospheric pressure at 800 °C. For the uncoated alloy sample (Fig. 9a), the surface is rather homogeneous and the oxide scale looks very thick. The oxide grains have a hexagonal shape. This particular microstructure is also different from that observed on Crofer 22 APU. The XRD analyses (Table 4) confirm that the oxide scale is mainly composed of chromia Cr_2O_3 and shows the presence of a spinel $(Cr,Fe)_3O_4$ very closed to $Cr_{1.3}Fe_{0.7}O_3$ (ICDD card no. 35-1112).

SEM cross-section (Fig. 10) observations show that the oxide scale is approximately 4 μm thick without any crack or gap at the interface oxide/alloy. The scale is composed of three layers: a near surface scale of 1.2 μm rich in chromium and manganese (mixture of a spinel oxide and chromia), a second layer of 800 nm rich in chromium and iron (mixture of Cr_2O_3 and spinel $(Cr,Fe)_3O_4$) and a third layer of 2 μm rich in chromium, iron and aluminium (mixture of Cr_2O_3, $(Cr,Fe)_3O_4$ and Al_2O_3). No silicon could be detected by EDX.

The morphology of the coated samples after 100 h at 800 °C is completely different from that observed on the uncoated sample. In the case of La_2O_3-coated AL 453, the morphology is similar to that observed in the case of La_2O_3-coated Crofer 22 APU. The oxide layers seem to be thinner as substrate grain boundaries remained visible on the oxidised surface. On the top surface, there is a spinel oxide covering a widely developed underscale of

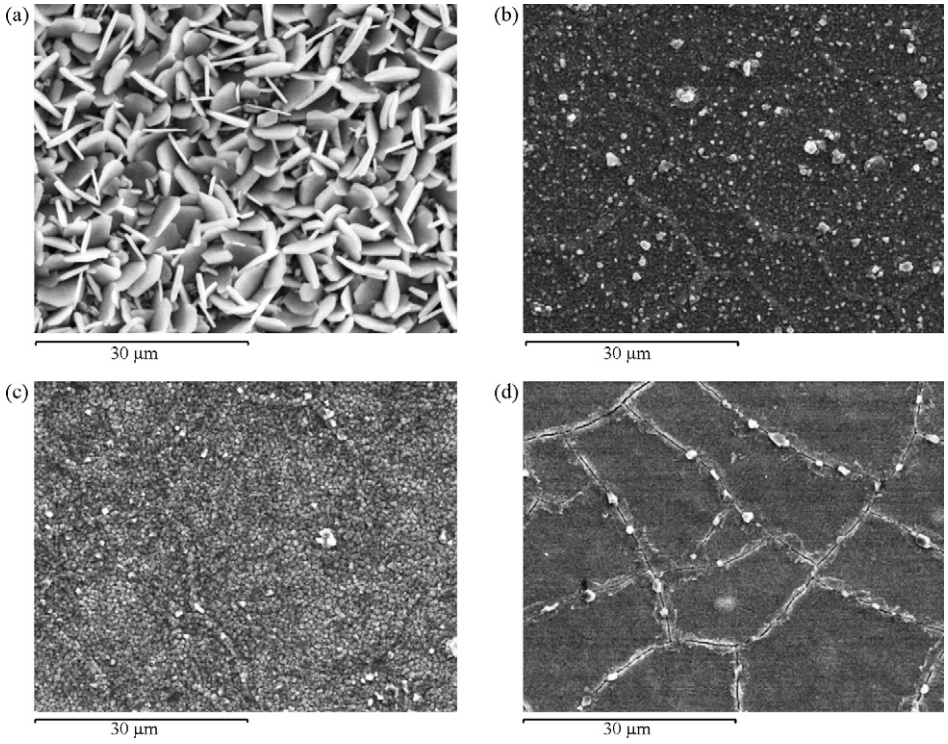

Fig. 9. SEM observations of AL 453 oxidized in air at 800 °C for 100 h: (a) without coating, (b) with La_2O_3 coating, (c) with Nd_2O_3 coating and (d) with Y_2O_3 coating.

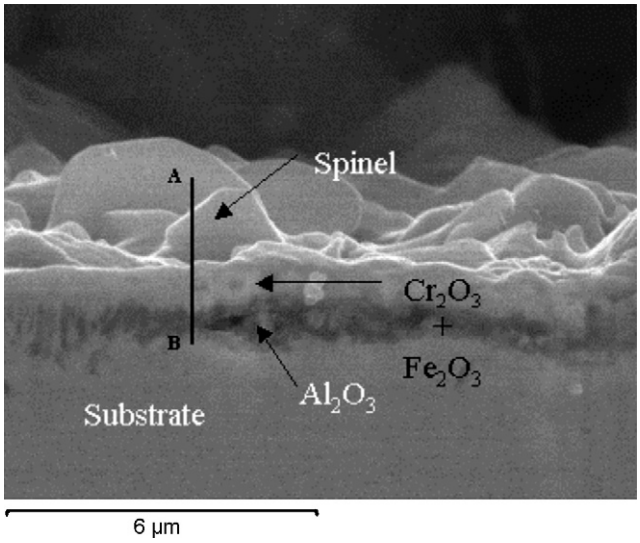

Fig. 10. Uncoated AL 453 oxidized 100 h at 800 °C: SEM cross-section image.

smaller grains of $LaCrO_3$. A spinel $(Cr,Mn)_3O_4$ and a perovskite of $LaCrO_3$ are detected by XRD.

Even if the Nd_2O_3 coating seems to have a weaker effect than that of the La_2O_3 coating, the morphology (Fig. 9c) and the nature of the crystalline phases (Table 4) are similar to those obtained for La_2O_3-coated AL 453. However, the deepest layer is made up of finer grains and enriched out with aluminium and silicon.

As Y_2O_3-coated Crofer 22 APU, Y_2O_3-coated AL 453 presents many cracks on the surface after 100 h at 800 °C (Fig. 9d). On these cracks, there are some spinel (enriched in Mn and Cr) grains. In addition, near these cracks, it is possible to observe a second layer rich in yttrium and chromium. A perovskite oxide $YCrO_3$ (ICDD card no. 34-0366) and a spinel $(Cr,Mn)_3O_4$ are identified by XRD, but the deposited yttrium oxide, Y_2O_3, remains the most important oxide (Table 4).

The ASR parameter depends on the selected coating (Fig. 11). In the case of the uncoated alloy, after 100 h at 800 °C in air, the ASR parameter is equal to 0.077 Ω cm^2. In the case of Y_2O_3 coating there is a small improvement of the electric conductivity, the value of the ASR being equal to 0.069 Ω cm^2. However, the value found for the Nd_2O_3 coating is higher, 0.524 Ω cm^2. In the case of La_2O_3, the value of the ASR parameter (0.219 Ω cm^2) is higher than that of the uncoated specimen. In addition, the curve in this last case presents many important variations.

3.3. Oxidation behaviour of uncoated and coated Haynes 230

Fig. 12 shows the mass gain of coated and uncoated Haynes 230 as a function of oxidation time. The weight change of uncoated specimen was similar to that of coated specimens but much lower than that of Crofer 22 APU and AL 453. The beneficial effect of reactive element is not so clearly visible. The oxidation behaviour is improved only in the case of La_2O_3 coating. In fact, the mass gain, if compared with the uncoated sample, is reduced of approximately 21% for the La_2O_3-coated specimen (Table 3). The oxidation kinetics of Haynes 230 is close to a parabolic rate law, even if the shape of the weight curves looks very wavy.

The morphology of the uncoated sample after 100 h at 800 °C shows a very fine oxide scale on the surface (Fig. 13a). Two layers can be distinguished: the deepest layer consists of very fine grains of chromia, whereas on the surface, crystals rich in chromium and nickel looking like a spinel phase are present. Large plates (2–3 µm) rich in tungsten are also present on the surface.

XRD analyses show that the oxide scale is mainly made of chromia and of a spinel oxide, $(Ni,Cr)_3O_4$ very closed to (Table 4). No silicon could be detected by EDX.

The morphology of the La_2O_3-coated (Fig. 13b) specimen is different from that of the uncoated sample. The layer is relatively homogeneous and compact; the oxide grains are smaller and appear less geometrical. As previously, plates rich in tungsten are present on surface corresponding to a tungsten oxide (WO_3) (ICDD card no. 75-2187) (Table 4), as confirmed by the XRD analysis. This analysis also reveals the presence of chromia, a spinel $(Ni,Cr)_3O_4$ and a perovskite $LaCrO_3$.

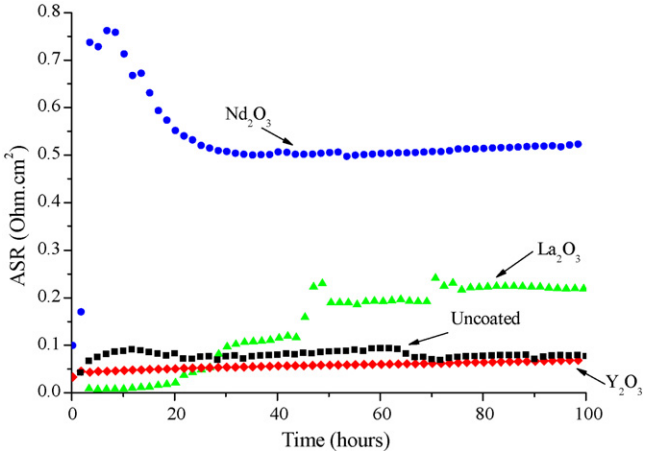

Fig. 11. ASR parameter evolution (for 100 h) of coated and uncoated AL 453 at 800 °C in air under atmospheric pressure.

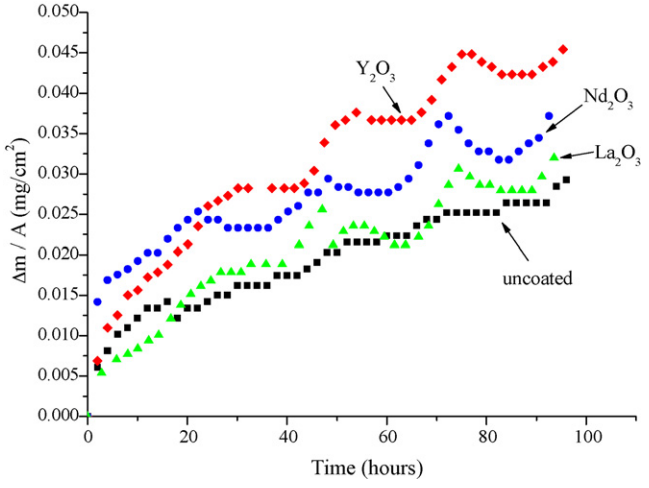

Fig. 12. Kinetics (for 100 h) of coated and uncoated Haynes 230 at 800 °C in air under atmospheric pressure.

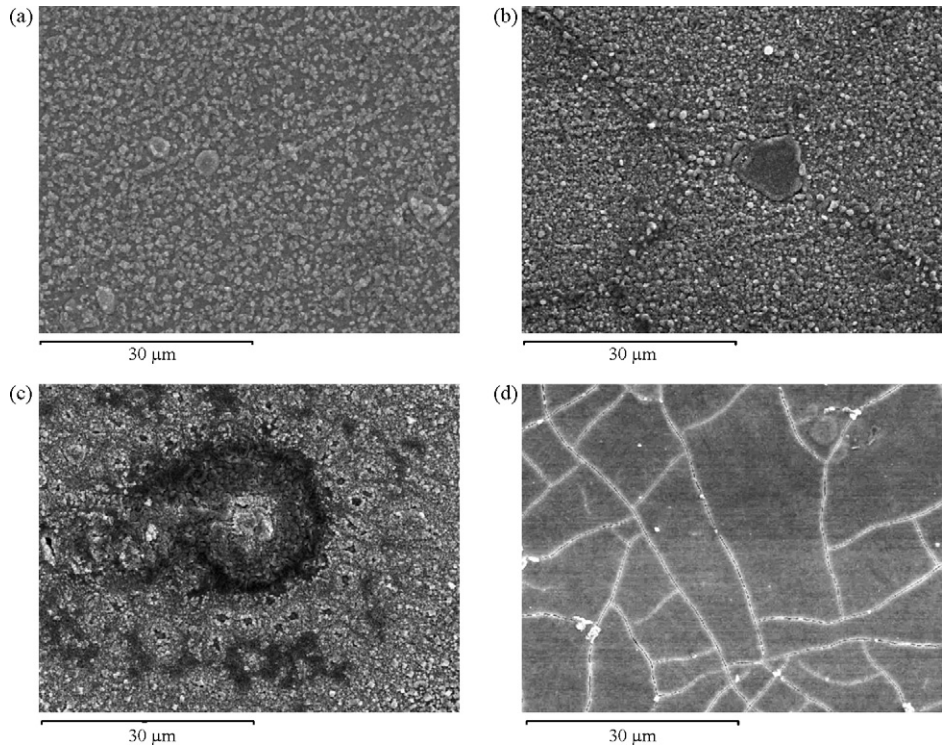

Fig. 13. SEM observations of Haynes 230 oxidized in air at 800 °C for 100 h: (a) without coating, (b) with La_2O_3 coating, (c) with Nd_2O_3 coating and (d) with Y_2O_3 coating.

In the case of Nd_2O_3-coated specimen, the morphology is slightly different (Fig. 13c). Indeed small craters with a dimension of 40 μm, in which are present tungsten and neodymium, are visible. The reminder of the surface is covered with a fine homogeneous layer of cubic crystals, overhanging a layer of smaller grains of chromia. The XRD analysis detects chromia and a perovskite phases $NdCrO_3$ (ICDD card no. 39-1429) (Table 4).

As in the case of ferritic alloys, the surface of the Y_2O_3-coated Haynes 230 presents many cracks (Fig. 13d). Those are very little decorated by spinel crystals. A perovskite phase $YCrO_3$, chromia and especially yttria are characterized by XRD (Table 4).

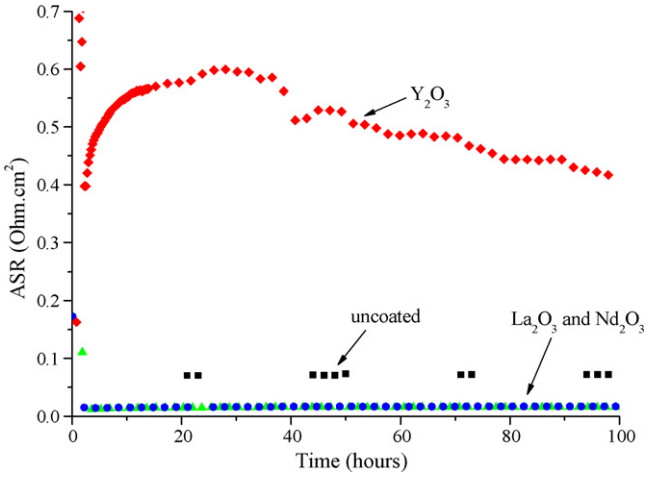

Fig. 14. ASR parameter evolution (for 100 h) of coated and uncoated Haynes 230 at 800 °C in air under atmosphere pressure.

Despite the small difference observed in thermogravimetry tests, the presence of a reactive element oxide on the surface of Haynes 230 modifies the value of ASR parameter compared to uncoated alloy (Fig. 14). For uncoated alloy after 100 h at 800 °C, the ASR parameter is equal to 0.072 Ω cm^2. The La_2O_3 coating and the Nd_2O_3 coating improve the electrical conductivity of the oxide layer. Actually after 100 h at 800 °C, the ASR parameter is equal to 0.016 Ω cm^2 for both coatings. However, as in the case of Crofer 22 APU, the value found for the Y_2O_3 coating is much higher, as it is equal to 0.398 Ω cm^2.

4. Discussion

The aim of this study was to determine the effects of reactive element oxides on the oxidation behaviour of two ferritic steels (Crofer 22 APU and AL 453) and a Ni-based alloy (Haynes 230). This study showed that the oxide growth followed parabolic kinetics. The Haynes 230 alloy, which is a Ni-base super alloy displays the best behaviour compared to ferritic alloys. But, one of important parameters that must satisfy an interconnect is its thermal expansion coefficient (TEC) which must be close to that of the others components of the cell. Haynes 230 offers a good corrosion resistance, but its TEC is higher (Table 5) than that of the other components of the cell; so, its use as an interconnect does not seem to be suitable, at least with classical electrodes and electrolyte materials.

In the case of Crofer 22 APU and of Haynes 230, the kinetic curves show important waves. This phenomenon can be due to the volatilisation of chromium oxides or tungsten oxides (only for Haynes 230). The local cracking of the oxide scale followed

Table 5
Material properties [2]

Materials	Thermal expansion coefficient (25–1000 °C) (10^{-6} °C^{-1})	Electrical resistivity (Ω cm)
Al_2O_3	8	5×10^8 at 700 °C
Cr_2O_3	9.6	10^2 at 800 °C
YSZ	10.5	19
Ni-YSZ	11–12	–
$LaCrO_3$	9.5	2.9 at 1000 °C
Crofer 22 APU	12.2	5×10^{-5}
AL 453	12.3	7.3×10^{-5}
Haynes 230	15.2	1.25×10^{-4}
Y_2O_3	–	10^{11} at 800 °C
$Cr_{1.5}Mn_{1.5}O_4$	7.5	20

by its healing can also explain this phenomenon which was already observed at higher temperature [47]. The TEM observations of uncoated Crofer 22 APU show the presence of these cracks between the substrate and the oxide scale: this illustrates the mechanism of formation of chromia by an outward diffusion of the chromium ions. Thus, vacancies are formed at the metal/oxide interface leading to scale cracking. This phenomenon of cracking–cicatrisation is very prejudicial for the behaviour and electric conductivity of oxide scale; moreover, it generates a rather important consumption of chromium.

The effects of reactive element oxide coatings are visible on morphologies after oxidation as well as on the oxidation kinetics. This study also shows that the effect of reactive element oxide coating is not universal, but depends on the nature of both coating and alloy. During the oxidation test at 800 °C in air of Crofer 22 APU, the mass gain, if compared with the uncoated sample, is reduced of 35% for the coated specimen. Furthermore, whatever the coating the volatilisation of chromium oxide and/or the cracking–cicatrisation phenomenon are reduced; in fact, the presence of reactive element on the surface seems to decrease the amplitude of waves on the kinetic curves. The TEM observations of La_2O_3-coated Crofer 22 APU suggest that the reactive element oxides act as a barrier limiting the outer Cr diffusion and, then reducing the ability for Cr VI compounds to evaporate and allowing the formation of the perovskite $LaCrO_3$. Thus, the changes in the diffusion mechanisms according to the addition of RE are clearly visible.

In the case of Haynes 230, the effect of coating is not clearly visible. The parabolic rate constants deduced from kinetic curves is unchanged and the volatilisation of chromium and tungsten oxide is still too important. In the past, Chevalier et al. [45] showed that the beneficial effects of reactive element in the chromia-forming alloys was due to the segregation of reactive element at chromia grain boundaries. In the case of Haynes 230, 100 h at 800 °C were probably not enough for the segregation of reactive element at the chromia-grain boundaries and then improving the corrosion resistance.

Generally, the yttrium oxide coating seems to have a different behaviour compared to the other reactive element coatings. The surface of all samples presents an homogeneously distributed presence of cracks. This phenomenon can be explained by a higher oxygen permeability in Y_2O_3 coating. The oxygen penetrates inside and forms a chromia scale at the interface between alloy and coating. This phenomenon was already observed on Y_2O_3-coated alumina forming materials [46,47] The chromia growth generates stresses and then creates some cracks in the Y_2O_3 coating, leading to chromium or manganese migration to the surface. Thus at 800 °C for 100 h, Y_2O_3 coatings do not react with chromia in order to form a perovskite $YCrO_3$. This delay was already observed at higher temperature [48].

In the past, it was showed by Hultquist et al. [49] that in oxide areas with Pt a pronounced inward oxygen transport and a substantial oxide growth near the substrate take place. But, after ASR measurements, SEM observations were made on the area with Pt. The scale morphology and composition in this area are exactly similar to that of areas without Pt.

The study of electric properties of oxide scale on uncoated Crofer 22 APU, AL 453 and Haynes 230 showed that these three alloys designed specifically for interconnect were well adapted. In fact, after 100 h at 800 °C the ASR parameter is close to 0.08 Ω cm^2 for all alloys; this value is lower than the limit of 0.1 Ω cm^2 generally reported in the literature [1–3]. However, after 40,000 h which is the target lifetime of these interconnects in fuel cells, an evaluation shows that this ASR parameter is equal to 0.9 Ω cm^2 for Crofer 22 APU, 1.0 Ω cm^2 for AL 453 and 1.1 Ω cm^2 for Haynes 230; these values are higher than 0.1 Ω cm^2 and not satisfactory for electrical conductivity. The evolution of electric properties of coated alloys depends on the reactive element and the metallic substrate. In the case of Y_2O_3-coated Crofer 22 APU, the Y_2O_3 coating is still present after 100 h at 800 °C. Its resistivity is very important, and higher than the resistivity of chromia and explains the increase of ASR parameter (ASR = 0.252 Ω cm^2). The presence of a perovskite like $LaCrO_3$ on Crofer 22 APU, improves the conductivity of the oxide scale: the ASR parameter is also equal to 0.004 Ω cm^2. Moreover, after 40,000 h, this parameter is evaluated to 0.035 Ω cm^2, which is still lower than 0.1 Ω cm^2. The perovskite phase is probably doped by iron ions which considerably improve the perovskite phase conductivity [50]. In comparison, Alman and Jablonski [33] found a ASR parameter equal to 0.07 Ω cm^2 after 500 h at 800 °C on Ce-coated Crofer 22 APU and Chen et al. [29] found a ASR parameter equal to 0.0025 Ω cm^2 after 200 h at 850 °C of (Mn,Co)-spinel coated Crofer 22 APU; but this value is predicted to reach of approximately 0.5 Ω cm^2 after 50,000 h at 850 °C [38]; which is too high to be used as interconnects. Contrary to Crofer 22 APU, the Y_2O_3-coated AL 453 forms a perovskite phase made of $YCrO_3$ after 100 h at 800 °C; this also explains the decrease of the ASR parameter.

Current testing is underway to assess the effectiveness of these treatments over a longer time period, in order to validate the present results after longer exposures.

The temperature of 800 °C looks somewhat too low to guarantee the formation of perovskite oxides and thus to improve the conductivity. In fact, the analysis made by XRD revealed that for Y_2O_3 coating, perovskite oxides were not formed after oxidation in air at 800 °C for 100 h. Preliminary treatments could be envisaged on coated samples in order to form perovskite phases: they could be heat-treated for 2 h at 1000 °C in air at atmospheric

pressure. The so-prepared perovskite could be tested in thermobalance and conductivity measurement could be performed in order to compare with the present work. The still open question is to know if it is better to pre-cover the surface of the alloy with a perovskite layer or to let its formation during the ageing of the material in the service conditions of SOFC.

In this study, the experiments were made exclusively in air at atmospheric pressure (cathode side). However, an interconnect has a anode side, in which it is exposed to hydrogen and steam. Also, experiments performed in H_2/10% H_2O at atmospheric pressure at 800 °C are actually in progress to validate the coatings influence from the anode side as well as the cathode side.

5. Conclusion

Crofer 22 APU, AL 453 and Haynes 230 alloys seem particularly suitable as interconnect in SOFC devices. The beneficial effects of reactive elements on oxidation behaviour were clearly visible. However, the conductivity of oxide scales was sometimes higher than that of uncoated samples. The coatings composed of a thin reactive element oxide such as, La_2O_3, Nd_2O_3 and Y_2O_3 resulted in an important improvement in the high temperature oxidation resistance; the oxide growth rate decreased, the adhesion between alloy and oxide scale is improved. The MOCVD method showed good reproducibility and excellent efficiency to obtain nanometric layers on the interconnect surface.

The first objective of these coatings was to form perovskite oxide with the chromia growing layer because perovskite present better conductivities than chromia, especially when they are doped with iron. The La_2O_3-coated Crofer 22 APU has the best electrical conductivity, in fact after 100 h at 800 °C, the ASR parameter is only 0.004 Ω cm^2 and the perovskite $LaCrO_3$ is the most important phase. Moreover, after 40,000 h, this parameter is evaluated to 0.035 Ω cm^2, which still lower than 0.1 Ω cm^2.

References

[1] W.Z. Zhu, S.C. Deevi, Mater. Res. Bull. 38 (2003) 957–972.
[2] W.Z. Zhu, S.C. Deevi, Mater. Sci. Eng. A348 (2003) 227–243.
[3] V. Shemet, J. Piron-Abellan, W.J. Quadakkers, L. Singheiser, in: N. Sammes, A. Smirnova, O. Vasylyev (Eds.), Fuel Cell Technologies: State and Perspectives, Springer, Netherlands, 2005, pp. 97–106.
[4] L. Antoni, Mater. Sci. Forum 461–464 (2004) 1073–1090.
[5] I. Kosacki, C.M. Rouleau, P.F. Becher, J. Bentley, D.H. Lowndes, Solid State Ionics 176 (2005) 1319–1326.
[6] F. Mauvy, J.-M. Bassat, E. Boehm, J.-P. Manaud, P. Dordor, J.-C. Grenier, Solid State Ionics 158 (2003) 17–28.
[7] J.W. Fergus, Mater. Sci. Eng. A397 (2005) 271–283.
[8] K. Huang, P.Y. Hou, J.B. Goodenough, Solid State Ionics 129 (2000) 237–250.
[9] N. Oishi, Y. Yamasaki, Electrochimical Society Proceedings, vol. 19, 1999, pp. 759–766.
[10] P. Berthod, Oxid. Met. 64 (2005) 235–252.
[11] H. Asteman, J.-E. Svensson, L.-G. Johansson, M. Norell, Oxid. Met. 52 (1999) 95–111.
[12] B.B. Ebbinghuaus, Combust. Flame 93 (1993) 119–137.
[13] T. Brylewski, M. Nanko, T. Maruyama, K. Przybylski, Solid State Ionics 143 (2001) 131–150.
[14] W.J. Quadakkers, J. Piron-Abellan, V. Shemet, L. Singheiser, Mater. High Temp. 20 (2) (2003) 115–127.
[15] M. Han, S. Peng, Z. wang, Z. Yang, X. Chen, J. Power Sources 164 (2007) 278–283.
[16] G.R. Holcomb, D.E. Alman, Scripta Mater. 54 (2006) 1821–1825.
[17] Z. Yang, M.S. Walker, P. Singh, J.W. Stevenson, T. Norby, J. Electrochem. Soc. 151 (2004) B669–B678.
[18] J.E. Hammer, S.J. Laney, R.W. Jackson, K. Coyne, F.S. Pettit, G.H. Meier, Oxid. Met. 67 (2007) 1–38.
[19] P.Y. Hou, J. Stringer, Mater. Sci. Eng. A202 (1995) 1–10.
[20] T. Brylewski, K. Przybylski, J. Morgiel, Mater. Chem. Phys. 81 (2003) 434–437.
[21] G. Cabouro, G. Caboche, S. Chevalier, P. Piccardo, J. Power Sources 156 (2006) 39–44.
[22] P. Piccardo, S. Chevalier, R. Molins, M. Viviani, G. Caboche, A. Barbucci, M. Sennour, R. Amendola, Surf. Coat. Technol. 201 (2006) 4471–4475.
[23] S. Chevalier, P. Dufour, G. Bonnet, J.C. Colson, Oxid. Met. 50 (1998) 27–49.
[24] A. Barbucci, P. Piccardo, M.P. Carpanese, M. Viviani, in: Z. Stoynov, D. Vladikova (Eds.), Portable and Emergency Energy Sources, Prof. Marin Drinov Academic Publishing House, Sofia, 2006, pp. 329–359.
[25] M. Stanislowski, J. Froitzheim, L. Niewwolak, W.J. Quadakkers, K. Hilpert, T. Markus, L. Singheiser, J. Power Sources 164 (2007) 578–589.
[26] Z. Yang, G. Xia, G.D. Maupin, J.W. Stevenson, Surf. Coat. Technol. 201 (2006) 4476–4483.
[27] J.-H. Kim, R.-H. Song, S.-H. Hyum, Solid State Ionics 174 (2004) 185–191.
[28] J.H. Zhu, Y. Zhang, A. Basu, Z.G. Lu, M. Paranthaman, D.F. Lee, E.A. Payzant, Surf. Coat. Technol. 177–178 (2004) 65–72.
[29] X. Chen, P.Y. Hou, C.P. Jacobson, S.J. Visco, L.C. De Jonghe, Solid State Ionics 176 (2005) 425–433.
[30] C. Collins, J. Lucas, T.L. Buchanan, M. Kopczyk, A. Kayani, P.E. Gannon, M.C. Deibert, R.J. Smith, D.-S. Choi, V.I. Gorokhovsky, Surf. Coat. Technol. 201 (2006) 4467–4470.
[31] M. Reza Bateni, P. Wei, X. Deng, A. Petric, Surf. Coat. Technol. 201 (2007) 4677–4684.
[32] W. Qu, J. Li, D.G. Ivey, J. Power Sources 138 (2004) 162–173.
[33] D.E. Alman, P.D. Jablonsski, Int. J. Hydrogen Energy (2006), doi:10.1016/j.ijhydene.2006.08.032.
[34] S. Chevalier, G. Bonnet, G. Brochardt, J.C. Colson, J.P. Larpin, Mater. Sci. Forum 369–372 (2001) 327–336.
[35] Z. Yang, G. Xia, J.W. Stevenson, J. Power Sources 160 (2006) 1104–1110.
[36] S.J. Geng, J.H. Zhu, Z.G. Lu, Solid State Ionics 177 (2006) 559–568.
[37] L. Jian, P. Jian, X. Jianzhong, Q. Xiaoliang, J. Power Sources 139 (2005) 182–187.
[38] S. Chevalier, G. Bonnet, J.P. Larpin, Appl. Surf. Sci. 167 (2000) 125–133.
[39] C. Houngninou, S. Chevalier, J.P. Larpin, Appl. Surf. Sci. 236 (2004) 256–269.
[40] K. Eisentrant, R.E. Sievers, J. Am. Chem. Soc. 20 (1965) 5254–5256.
[41] B. Pierragi, Oxid. Met. 27 (1987) 177–185.
[42] P. Huczkowski, N. Christiansen, V. Shemet, J. Piron-Abellan, L. Singheiser, W.J. Quadakkers, Mater. Corros. 55 (2004) 825–830.
[43] W.J. Quadakkers, J. Piron-Abellan, V. Shemet, Mater. Res. 7 (2004) 203–208.
[44] Z. Yang, K. Scott Weil, D.M. Paxton, J.W. Stevenson, J. Electrochem. Soc. 150 (2003) A1188–A1201.
[45] S. Chevalier, G. Bonnet, K. Przybylski, J.C. Colson, J.P. Larpin, Oxid. Met. 54 (2000) 527–547.
[46] S. Chevalier, J.P. Larpin, Acta Mater. 50 (2002) 3105–3114.
[47] S. Chevalier, C. Nivot, J.P. Larpin, Oxid. Met. 61 (2004) 195–217.
[48] K. Przybylski, T. Brylewski, J. Morgiel, Mater. Sci. Forum 461–464 (2004) 1099–1106.
[49] G. Hultquist, E. Hörnlund, Q. Dong, Corros. Sci. 45 (2003) 2697–2703.
[50] N. Sakai, T. Horita, Y.P. Xiaong, K. Yamaji, H. Kishimoto, M.E. Brito, H. Yokokawa, T. Maruyama, Solid State Ionics 176 (2005) 681–686.